Astron. Astrophys. 363, 1123–1133 (2000)

ASTRONOMY
AND
ASTROPHYSICS

Far-infrared [C II]/continuum ratio toward the central kiloparsecs of M31⋆

Comparison with that of our Galaxy

K. Mochizuki⋆⋆

Department of Astronomy, University of Tokyo, Japan (mochi@ir.isas.ac.jp)

Received 21 April 2000 / Accepted 19 September 2000

Abstract. We observed the nearby spiral galaxy M31 with the Long-Wavelength Spectrometer on board the Infrared Space Observatory. Far-infrared line-to-continuum ratios of $[\mathrm{C\,II}]/100\ \mu\mathrm{m} \simeq 6 \times 10^{-3}$ were obtained for the central kiloparsec region along the major axis of the galaxy. These ratios are 2–3 times higher than those in the Galactic counterpart and are closer to those in the general Galactic plane. This indicates that the gas-to-dust heating ratio of the neutral interstellar medium in the center of M31 is not affected by the soft interstellar radiation field due to the late-type stars in the bulge. Comparing the observations with photon-dominated region models, we conclude that the molecular clouds in the central region of M31 are translucent (the mean hydrogen column density of each cloud is $\langle N_{\mathrm{H}} \rangle \lesssim 10^{21}\ \mathrm{cm}^{-2}$) for photons sufficiently energetic to heat the dust grains but not the gas. The smaller column density of the M31 clouds could result from a lower molecular-gas density suggested by previous millimeter observations. The lower recent star-forming activity in the inner part of M31 is likely to cause a lower pressure of the interstellar medium, and then the lower gas density.

Key words: ISM: general – Galaxy: center – galaxies: individual: M31 – galaxies: ISM – infrared: ISM: lines and bands

1. Introduction

The [C II] 158 μm ($^2P_{3/2} \rightarrow {}^2P_{1/2}$) line emission often dominates the gas cooling in the neutral phase of the interstellar medium (ISM). This makes the line strength trace the heating rate of the interstellar neutral gas in a steady state. Nakagawa et al. (1998) observed the Galactic plane in the [C II] emission to obtain a nearly constant intensity ratio of $I_{[\mathrm{C\,II}]}/I_{40-120\,\mu\mathrm{m}} \simeq 6 \times 10^{-3}$, where $I_{[\mathrm{C\,II}]}$ is the velocity-integrated [C II] intensity and $I_{40-120\,\mu\mathrm{m}}$ is the continuum intensity integrated at $40\ \mu\mathrm{m} \leq \lambda \leq 120\ \mu\mathrm{m}$ derived from Infrared Astronomical Satellite ($IRAS$) data. Since the far-infrared (FIR) continuum emission traces the cooling of dust grains, the observations indicate that the heating ratio of gas-to-dust is nearly constant on a galactic scale.

However, Nakagawa et al. (1995; hereafter Paper I) obtained a lower intensity ratio of $I_{[\mathrm{C\,II}]}/I_{40-120\,\mu\mathrm{m}} \simeq 2 \times 10^{-3}$ toward the central kiloparsec region of our Galaxy. They ascribed this lower line-to-continuum ratio to the softer interstellar radiation field in the Galactic center. The gas-heating in the [C II]-emitting regions is primarily due to electrons ejected from dust grains hit by ultraviolet (UV) photons (e.g., $h\nu \geq 6$ eV; de Jong et al. 1980), while the grains themselves are heated by less energetic photons in the optical to near-infrared as well as UV photons. The central kiloparsec region of our Galaxy is rich in photons sufficiently energetic to heat the dust grains but not sufficient to heat the gas owing to dominance of the late-type stars in the Galactic bulge. This leads to a smaller gas/dust heating ratio, and thus to the smaller FIR [C II]/continuum intensity ratio (Paper I).

Extragalactic observations help us to further investigate influence of a soft incident radiation field on the gas-to-dust heating ratio of the ISM. For this purpose, we selected the central kiloparsecs of the nearby spiral galaxy M31, which has a bright bulge (e.g., Martinez Roger et al. 1986) containing a large amount of late-type stars. In this paper we report FIR spectroscopic observations toward the M31 central region. We adopt a distance to M31 of $D_{\mathrm{M31}} = 690$ kpc. At this distance, an angular distance of $60''$ corresponds to 200 pc.

2. Observations and data reduction

We observed M31 in a wavelength range of $43\ \mu\mathrm{m} \leq \lambda \leq 188\ \mu\mathrm{m}$ with the Long-Wavelength Spectrometer (LWS; Clegg et al. 1996) on board the Infrared Space Observatory (ISO; Kessler et al. 1996). The observations comprised three one-dimensional raster scans with the Target Dedicated Time (TDT) numbers 58002001, 58302603, and 60202005. The combination of these raster scans results in a strip map of 31 positions

⋆ Based on observations with ISO, an ESA project with instruments funded by ESA member States (especially the PI countries: France, Germany, the Netherlands and the United Kingdom) and with the participation of ISAS and NASA.

⋆⋆ *Present address:* Infrared Astrophysics Division, The Institute of Space and Astronautical Science, 3-1-1 Yoshinodai, Sagamihara, Kanagawa 229-8510, Japan

along the major axis (the position angle is $38°$) of the galaxy centered on the galactic nucleus at $\alpha(2000) = 00^{\rm h}42^{\rm m}44\overset{\rm s}{.}4$ and $\delta(2000) = 41°16'08\overset{''}{.}5$. The observed positions were spaced at $50''$, with offsets of $-750'' \leq x \leq +750''$ relative to the galactic nucleus ($-750'' \leq x \leq -300''$ in TDT 58302603, $-250'' \leq x \leq +250''$ in TDT 58002001, and $+300'' \leq x \leq +750''$ in TDT 60202005; x is positive in the northeast).

We adopted the Astronomical Observation Template (AOT) LWS01 mode: grating spectroscopy with a medium-resolution of $\Delta\lambda = 0.3\ \mu$m at $43\ \mu{\rm m} \leq \lambda \leq 90\ \mu$m and $\Delta\lambda = 0.6\ \mu$m at $84\ \mu{\rm m} \leq \lambda \leq 188\ \mu$m. The observations at each of the raster position consisted of 4 grating scans, with 1.6 seconds of total integration time for each grating position. The grating positions were spaced at 1/2 of the spectral resolution.

The beam size of the LWS derived from observations of Mars was $74''$ and $68''$ in FWHM averaged over position angle for the detectors LW1 (around $\lambda = 100\ \mu$m) and LW4 (around $\lambda = 158\ \mu$m), respectively (Lloyd 1999). The equivalent disks had nearly equal solid angles for the detectors LW1 and LW4: $\Omega = 1.3\times10^{-7}$ ster and 1.2×10^{-7} ster, respectively (Lloyd 1999).

We subtracted the detector dark currents from the Standard Processed Data (SPD) of Off-Line Processing (OLP) version 7.0 products, using the LWS Interactive Analysis[1] (LIA) version 7.2a and 7.3. The ISO Spectral Analysis Package[2] (ISAP) version 1.6a was used for the data reduction afterwards. The data affected by cosmic-ray hits were manually removed, when they had not been discarded automatically in the SPD. Then the dark current level of LW1 was reevaluated so that the spectrum is consistent between LW1 and LW2 at the overlapping wavelength region of the two detectors because LW1 has problems with dark-current measurements. We derived the [C II] flux from a single-Gaussian fit with a polynomial baseline of the first or second order. The width, height, and central velocity of the line profile were determined by the fit for a spectrum with a [C II] flux of $F_{\rm [C\,II]} \geq 10^{-19}$ W cm^{-2}. On the other hand, only the height and central velocity were determined by the fit for a $F_{\rm [C\,II]} < 10^{-19}$ W cm^{-2} spectrum; the width for the fit was fixed to that of the instrumental profile for such a spectrum with a limited signal-to-noise ratio. The continuum flux density, $f_\nu(100\ \mu{\rm m})$, at $\lambda = 100\ \mu$m was derived from the convolution of the LWS spectrum and the $IRAS$ $100\ \mu$m band transmission.

The flux calibration of the LWS grating mode was based on observations of Uranus (Swinyard et al. 1998) for point-like sources. This calibration is accurate to 15% when uncertainty concerned with extended-source correction and dark-current subtraction are excluded (Swinyard et al. 1998). In case of the continuum emission from faint (less than 100 Jy at $\lambda \simeq 100\,\mu$m) sources such as the central region of M31, the calibration uncertainty can be larger because the instability of detector dark-current often determines the calibration accuracy. This instability affects the calibration more significantly for raster scans than for single-point observations, since the instability is difficult to distinguish from spatial variation in source brightness. Thus, we evaluated the uncertainty in $f_\nu(100\ \mu{\rm m})$ on the basis of the present observations, by comparing the LWS data with the corresponding $IRAS$ data (Sect. 3.2).

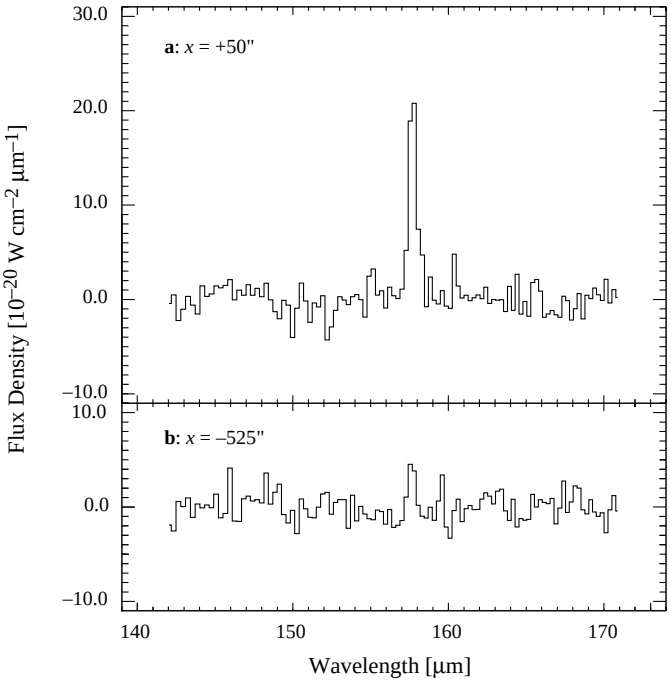

Fig. 1a and b. Representative [C II] line spectra observed along the major axis of M31. Second-order baselines were subtracted. **a** At $x = +50''$, detection. **b** Averaged at $x = -500''$ and $-550''$, non-detection.

3. Results

In the following presentation of our results, we focus on a comparison with the Galactic counterparts, especially for the $[{\rm C\,II}]/100\ \mu$m FIR line-to-continuum ratio.

3.1. [C II] line emission

The derived [C II] flux ($F_{\rm [C\,II]}$) is shown in Table 1 with the spatial offset x (positive in the northeast) relative to the nucleus of M31 along its major axis. The [C II] line was unresolved in each spectrum at the resolution. Thus, we discuss the line flux integrated over wavelength only. The listed uncertainty in $F_{\rm [C\,II]}$ represents statistical one (1σ) based on the residuals of the spectral fit at the baseline regions. The correction for an extended source is not adopted because the correction factor is not yet fixed (Swinyard et al. 1998). The uncertainty in this correction does not affect the $[{\rm C\,II}]/100\ \mu$m ratio (Sect. 3.3) based on the LWS observations significantly, because of the similar distributions (Sect. 3.2) of the two emissions. At an offset of $|x| \geq 300''$,

[1] The LWS Interactive Analysis (LIA) is a joint development of the ISO-LWS Instrument Team at RAL (the PI institute) and IPAC.

[2] The ISO Spectral Analysis Package (ISAP) is a joint development by the LWS and SWS Instrument Teams and Data Centers. Contributing institutes are CESR, IAS, IPAC, MPE, RAL and SRON.

Table 1. Observed FIR emission along the major axis of M31. For an offset of $|x| \geq 300''$, the average of two adjacent observed positions is listed. The line-to-continuum ratio is derived from the LWS line and continuum at $|x| \leq 250''$; the LWS line and HiRes continuum at $|x| \geq 300''$.

Offset x arcsec	[C II] flux[a] $F_{[\mathrm{C\,II}]}$ 10^{-20} W cm^{-2}	LWS 100 μm flux density[b] $f_\nu^{\mathrm{LWS}}(100\ \mu\mathrm{m})$ Jy	HiRes 100 μm intensity $I_\nu^{\mathrm{HiRes}}(100\ \mu\mathrm{m})$ MJy ster^{-1}	[C II]/100 μm ratio[c] $F_{[\mathrm{C\,II}]}/\nu f_\nu(100\ \mu\mathrm{m})$ 10^{-3}
-725	≤ 4.0	...	12.4	≤ 8.8
-625	≤ 3.5	...	11.4	≤ 8.5
-525	≤ 4.2	...	7.7	≤ 15.0
-425	≤ 3.3	...	7.2	≤ 12.6
-325	≤ 3.6	...	8.5	≤ 11.8
-250[d]	...	0.9	12.2	...
-200	7.0 ± 1.0	3.5	18.5	6.6 ± 1.9
-150	7.1 ± 0.7	4.5	30.7	5.3 ± 1.2
-100	10.8 ± 0.8	7.0	42.6	5.1 ± 0.8
-50	11.0 ± 1.4	6.1	52.3	6.0 ± 1.2
± 0	14.6 ± 1.2	7.7	58.1	6.3 ± 0.9
$+50$	14.5 ± 1.4	10.9	56.0	4.4 ± 0.6
$+100$	9.8 ± 0.7	7.0	50.0	4.6 ± 0.7
$+150$	7.3 ± 0.6	4.5	40.4	5.4 ± 1.1
$+200$	6.4 ± 0.7	4.9	28.1	4.3 ± 0.9
$+250$	4.0 ± 0.5	2.0	22.9	6.7 ± 3.2
$+325$	≤ 5.4	...	16.4	≤ 9.1
$+425$	3.7 ± 0.6	...	13.1	6.9 ± 2.4
$+525$	≤ 2.9	...	12.3	≤ 6.5
$+625$	≤ 3.4	...	11.8	≤ 7.8
$+725$	≤ 3.5	...	9.7	≤ 9.8

[a] The uncertainty represents statistical one (1σ). The upper limit corresponds to a 4σ level.
[b] The uncertainty is 0.9 Jy (1σ).
[c] The uncertainty includes that in the flux calibration of the LWS and HiRes observations at $|x| \geq 300''$.
[d] The line flux was not derived because of the contamination due to cosmic-ray hits.

where the line emission is weak, the average spectrum of two adjacent observed positions is analyzed to further reduce the noise.

We adopted a conservative upper limit of a 4σ level for a non-detection because a low-level signal is sometimes hard to separate from glitches due to cosmic-ray hits. Representative spectra are displayed in Fig. 1 for detection at $x = +50''$ and non-detection at $x = -525''$; the derived line flux for the latter is slightly below our 4σ criterion for detection. At $x = -250''$, we failed to derive the line flux because of the significant contamination due to cosmic-ray hits.

Fig. 2a shows the observed [C II] flux as a function of the offset x. The flux uncertainties and upper limits are equivalent to those in Table 1. The horizontal bars indicate the size of the spatial sampling profile: the FWHM ($68''$; Lloyd 1999) of the LWS beam at $|x| \leq 250''$; at $|x| \geq 300''$, the sum of the beam FWHM and the separation ($50''$) between the two adjacent averaged positions.

For comparison, we simulated LWS observations of our Galaxy located at the distance of M31, as also shown in Fig. 2. The [C II] map of Nakagawa et al. (1998) was regridded under the assumption $D_{\mathrm{M31}}/D_{\mathrm{Milky\,Way}} = 690\ \mathrm{kpc}/8.5\ \mathrm{kpc}$, where D_{M31} and $D_{\mathrm{Milky\,Way}}$ are the distances to the centers of M31 and our Galaxy, respectively. Then the map was convolved with a Gaussian profile, in order to produce the final spatial resolution equal to that of the LWS. Since the BICE observations have a possible offset of $I_{[\mathrm{C\,II}]} \simeq -2 \times 10^{-5}\ \mathrm{ergs\,s^{-1}\,cm^{-2}\,ster^{-1}}$ in the [C II] intensity (Nakagawa et al. 1998), the simulation is shown for the offset-corrected flux as well as that without the correction.

An extended [C II] component was detected over the central 1.6 kpc ($\Delta x \simeq 500''$) of M31, while upper limits were obtained at most of the outer regions, as shown in Fig. 2a. The [C II] emission observed in M31 is different from that in our Galaxy as follows:

1. The [C II] emission detected in M31 is fainter by one to two orders of magnitude.
2. The [C II] emission in M31 lacks a spatially unresolved nucleus component, which is obvious in our Galaxy.
3. The central kiloparsec region of M31 is brighter than its disk region just outside, while the Galactic center (except the nucleus component) is less bright (Paper I) than the Galactic disk shown.

Points 1 and 2 above may be accounted for by a smaller amount of the ISM and less active recent star formation in the inner disk and around the nucleus of M31. The weak emission in

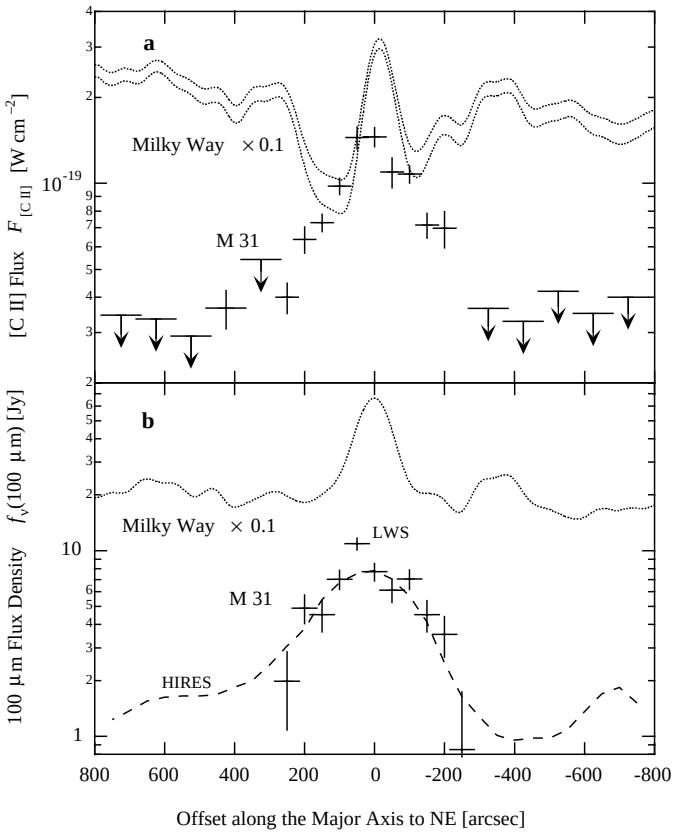

Fig. 2a and b. Distributions of FIR emission along the major axis of M31 (crosses; bars with arrows for upper limits), plotted as a function of the spatial offset x (positive in the northeast) relative to the nucleus of the galaxy. The M31 data are quoted from Table 1. The horizontal bars indicate the size (FWHM) of the spatial sampling profile. The dotted curves simulate our Galaxy (Nakagawa et al. 1998; the ISSA), located at the distance of M31 and observed with the LWS. The flux and flux density of our Galaxy were multiplied by 10^{-1}. Extended-source correction is not applied for the LWS nor $IRAS$ data. **a** [C II] 158 μm line flux ($F_{[C II]}$; this work). The upper dotted curve indicates the flux corrected for the possible offset of the Galactic observations. The lower dotted curve is for that without the correction. **b** Continuum flux density $f_\nu(100\ \mu\mathrm{m})$ at $\lambda = 100\ \mu$m. The dashed curve indicates $IRAS$ HiRes brightness in M31 multiplied by the solid angle of the LWS beam.

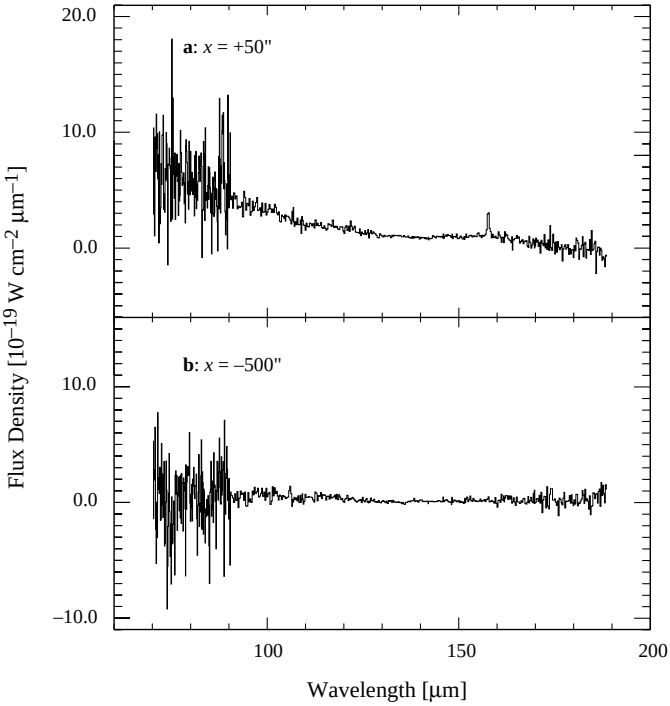

Fig. 3a and b. Representative spectra at a wavelength range of 70 $\mu\mathrm{m} \leq \lambda \leq 188\ \mu$m observed along the major axis of M31. **a** At $x = +50''$. **b** At $x = -500''$.

M31 was also pointed out in other tracers of the ISM, such as the FIR continuum (Walterbos & Schwering 1987), the CO ($J = 1$–0) line (Dame et al. 1993), and the H I 21 cm line (Brinks & Shane 1984).

3.2. 100 μm *continuum emission*

The continuum flux density, $f_\nu^{\mathrm{LWS}}(100\ \mu\mathrm{m})$, at $\lambda = 100\ \mu$m observed with the LWS is listed in Table 1. The LWS continuum data can be compared with the brightness $I_\nu^{\mathrm{HiRes}}(100\ \mu\mathrm{m})$ in the 100 μm band of the $IRAS$ High Resolution processing (HiRes; Rice 1993) data. The calibration correction for extended sources is not adopted for f_ν^{LWS} nor I_ν^{HiRes} (Wheelock et al. 1994). The distribution of the LWS 100 μm flux density is shown in Fig. 2b along with the HiRes flux density $I_\nu^{\mathrm{HiRes}}(100\ \mu\mathrm{m})\Omega^{\mathrm{LWS}}(100\ \mu\mathrm{m})$, where $\Omega^{\mathrm{LWS}}(100\ \mu\mathrm{m}) = 1.3 \times 10^{-7}$ ster (Lloyd 1999) is the effective solid angle of the LWS beam at 100 μm. The two datasets agree well at $|x| \leq 250''$ as shown in Fig. 2b, in spite of the slightly larger beam ($120'' \times 90''$ in FWHM) of the HiRes data. This is probably due to the relatively smooth distribution of the FIR emission in the observed regions and to the similarity in the extended-source correction factor between the two datasets.

We evaluated the uncertainty from the deviation of f_ν^{LWS} from $I_\nu^{\mathrm{HiRes}}\Omega^{\mathrm{LWS}}$ (Sect. 2) at $|x| \geq 300''$, where the difference in the beam sizes hardly affect the brightness because the distribution of the FIR emission is quite smooth as shown in Fig. 2b. The estimated uncertainty is 0.9 Jy (1σ) in $f_\nu^{\mathrm{LWS}}(100\ \mu\mathrm{m})$. This value is comparable to $I_\nu^{\mathrm{HiRes}}\Omega^{\mathrm{LWS}}$ at $|x| \geq 300''$, where this uncertainty was estimated; the estimated uncertainty is practically equivalent to the fluctuation in the derived $f_\nu^{\mathrm{LWS}}(100\ \mu\mathrm{m})$ at the background regions without detectable emission. Representative spectra at a wavelength range of 70 $\mu\mathrm{m} \leq \lambda \leq 188\ \mu$m are displayed in Fig. 3 for detection at $x = +50''$ and non-detection at $x = -500''$; the emission at shorter wavelengths does not contribute to $f_\nu^{\mathrm{LWS}}(100\ \mu\mathrm{m})$ discussed in the present paper.

The 100 μm emission is distributed similarly to the [C II] emission in M31 as shown in Fig. 2. The central component has a width of $\simeq 1.6$ kpc ($500''$), approximately equal to that of the [C II] emission. For comparison, the simulation of our Galaxy located at the distance of M31 is shown for the 100 μm continuum (the $IRAS$ Sky Survey Atlas; ISSA) in Fig. 2b, as for the

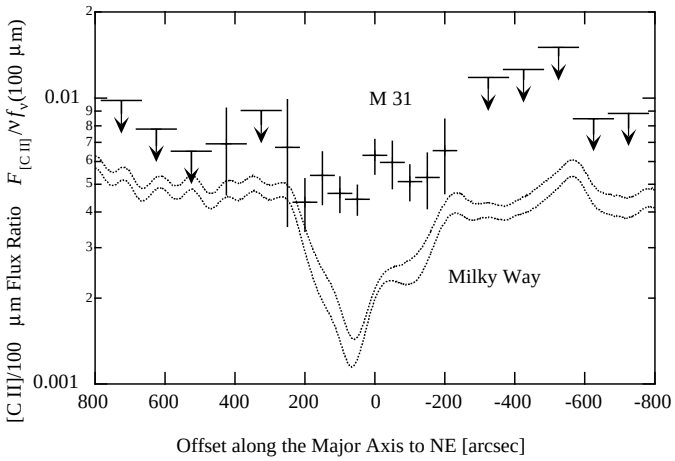

Fig. 4. Distribution of the FIR $[\mathrm{C\,II}]/100\ \mu\mathrm{m}$ line-to-continuum ratio along the major axis of M31 (crosses; bars with arrows for upper limits), plotted as a function of the spatial offset x relative to the nucleus of the galaxy. The M31 ratios with the uncertainties are from Table 1. The horizontal bars indicate the size (FWHM) of the spatial sampling profile. The dotted curves simulate our Galaxy (Nakagawa et al. 1998; the ISSA), located at the distance of M31 and observed with the LWS beam. The two dotted curves correspond to the cases with and without the correction for the possible [C II] offset, as in Fig. 2a. For derivation of the Galactic ratios, the extended-source correction was applied to the $100\ \mu\mathrm{m}$ emission.

[C II] line in Fig. 2a. Extended-source correction for the ISSA (Wheelock et al. 1994) is not applied to Fig. 2b. In contrast to M31, the line and continuum FIR distribution is quite different in our Galaxy: the $100\ \mu\mathrm{m}$ emission lacks the depression in the central kiloparsec seen in the [C II] emission.

3.3. [C II]/100 μm ratio

The FIR line-to-continuum flux ratio of $F_{[\mathrm{C\,II}]}/\nu f_\nu(100\ \mu\mathrm{m})$ is derived from the LWS data at $|x| \leq 250''$ (Table 1). The uncertainty in the ratio at these positions is based on those in $F_{[\mathrm{C\,II}]}$ and $f_\nu^{\mathrm{LWS}}(100\ \mu\mathrm{m})$ listed in Table 1. On the other hand, at $|x| \geq 300''$ the LWS continuum data have insufficient signal-to-noise ratios. Since the FIR brightnesses at these positions are hardly affected by the difference in beam sizes because of the smooth distribution of the emission (Fig. 2b), we took instead the ratio to the HiRes data there: $F_{[\mathrm{C\,II}]}/\nu f_\nu(100\ \mu\mathrm{m}) = F_{[\mathrm{C\,II}]}/\left[\nu I_\nu^{\mathrm{HiRes}}(100\ \mu\mathrm{m})\Omega^{\mathrm{LWS}}(100\ \mu\mathrm{m})\right]$. In this case, the uncertainty in the $[\mathrm{C\,II}]/100\ \mu\mathrm{m}$ ratio includes the flux calibration uncertainties of the two different instruments (15% for the [C II], Sect. 2; 10% for $100\ \mu\mathrm{m}$, Xu & Helou 1994), as well as the statistic uncertainty in $F_{[\mathrm{C\,II}]}$.

The distribution of $F_{[\mathrm{C\,II}]}/\nu f_\nu(100\ \mu\mathrm{m})$ in M31 is plotted in Fig. 4. The ratio is $F_{[\mathrm{C\,II}]}/\nu f_\nu(100\ \mu\mathrm{m}) \simeq 6 \times 10^{-3}$ for the central kiloparsec of M31. The upper limits for the outer regions are consistent with a constant ratio of $F_{[\mathrm{C\,II}]}/\nu f_\nu(100\ \mu\mathrm{m}) \simeq 6 \times 10^{-3}$ through the observed regions in M31. This distribution is in contrast to the Galactic distribution also shown in Fig. 4. For derivation of the Galactic ratios, the extended-source correction was applied to the ISSA data: the $100\ \mu\mathrm{m}$ flux was multiplied by 0.72 (Wheelock et al. 1994). Our Galaxy has a nearly constant ratio of $F_{[\mathrm{C\,II}]}/\nu f_\nu(100\ \mu\mathrm{m}) \simeq 5 \times 10^{-3}$ in the disk, with 2–3 times lower $F_{[\mathrm{C\,II}]}/\nu f_\nu(100\ \mu\mathrm{m}) \simeq 2 \times 10^{-3}$ in the central kiloparsec, as reported in Paper I. The ratios in the central kiloparsec of M31 are 2–3 times higher than those in the Galactic counterpart and closer to those in the Galactic disk outside. In the outer regions, no difference between the galaxies is found.

The lower ratios observed in our Galactic center were ascribed to the radiation from late-type stars in the Galactic bulge (Paper I): the soft radiation illuminating the neutral ISM heats the dust grains, but does not heat the gas effectively (de Jong et al. 1980). However, the central kiloparsec of M31 does not show low $[\mathrm{C\,II}]/100\ \mu\mathrm{m}$ ratios, in spite of its bright (e.g., Martinez Roger et al. 1986) bulge.

4. Discussion

The [C II] emission can originate in the neutral (e.g., Shibai et al. 1991) and ionized (e.g., Heiles 1994) phases of the ISM. When the neutral phase is considered, the nearly constant FIR [C II]-to-continuum ratio in the Galactic disk can be accounted for by a stable heating ratio of gas-to-dust as mentioned below (Sect. 4.1; also in Mochizuki & Nakagawa 2000). On the other hand, in the ionized phase, we do not find a reason for the stable line-to-continuum ratio because: (1) the [C II] emission is not the dominant coolant of the gas; (2) the gas is not heated via dust grains. Since the $F_{[\mathrm{C\,II}]}/\nu f_\nu(100\ \mu\mathrm{m})$ in the center of M31 is close to the nearly constant ratio in the Galactic disk, the [C II] emission there is likely to originate in the neutral phase. Thus, we discuss the different FIR [C II]/continuum flux ratios between the two galactic centers on the basis of Photon-Dominated Region (PDR) models, which are made for the neutral phase of the ISM.

4.1. Factors affecting the [C II]/100 μm ratio

When the ISM in a steady state is considered, the ratio of the [C II] flux to the FIR flux (F_{FIR}) integrated over wavelength can be written as:

$$\frac{F_{[\mathrm{C\,II}]}}{F_{\mathrm{FIR}}} = \eta_{[\mathrm{C\,II}]}\frac{\Gamma_{\mathrm{gas}}}{\Gamma_{\mathrm{dust}}}, \tag{1}$$

where $\eta_{[\mathrm{C\,II}]}$ is the fraction of the [C II] cooling in the total gas cooling, and Γ_{gas} and Γ_{dust} are heating rates of the gas and dust, respectively. The gas heating is usually dominated by energetic photoelectrons from grain surfaces illuminated by stellar light (de Jong 1977) in the neutral phase of the galactic ISM. In this case, the heating ratio of $\Gamma_{\mathrm{gas}}/\Gamma_{\mathrm{dust}}$ can be replaced by the efficiency ϵ_{ph} (Tielens & Hollenbach 1985), which is defined as the ratio of the energy carried away by the emitted photoelectrons to that absorbed by the grains, of the photoelectric heating as follows:

$$\frac{F_{[\mathrm{C\,II}]}}{F_{\mathrm{FIR}}} = \eta_{[\mathrm{C\,II}]}\epsilon_{\mathrm{ph}}. \tag{2}$$

The nearly constant $F_{[\mathrm{C\,II}]}/F_{\mathrm{FIR}}$ observed in the Galactic disk (Nakagawa et al. 1998) indicates that ϵ_{ph} is nearly constant and that the [C II] emission dominates the gas cooling ($\eta_{[\mathrm{C\,II}]} \simeq 1$), in wide ranges of physical conditions in the neutral phase of the Galactic ISM.

Although the $[\mathrm{C\,II}]/100\ \mu\mathrm{m}$ ratio is stable, it can be affected by several factors:

1. The color of the stellar light illuminating the ISM. Grains can be heated by photons not sufficiently energetic to produce a photoelectron from the grains. Thus, soft stellar radiation decreases the effective ϵ_{ph} for the whole wavelength range of the stellar light. This leads to a lower $[\mathrm{C\,II}]/100\ \mu\mathrm{m}$ ratio (Paper I).
2. The hydrogen column density of a cloud. At a lower column density, the cloud is translucent for less energetic incident photons. This increases the emergent $[\mathrm{C\,II}]/100\ \mu\mathrm{m}$ ratio to that of an opaque cloud illuminated by harder stellar radiation.
3. The charge of grains. When a grain is positively charged, further emission of a photoelectron requires more energy because of the opposite charges of the grain and electron (de Jong 1977). This decreases ϵ_{ph} and consequently decreases the $[\mathrm{C\,II}]/100\ \mu\mathrm{m}$ ratio. The grain charge is determined by the balance between the photoelectron emission and the grain–electron recombination. The emission rate of photoelectrons varies roughly as $I_{\mathrm{ph}}n$ while the recombination rate does as n^2, where I_{ph} is the intensity of the illuminating stellar radiation, and n is the gas density. Thus, the grains are positively charged at a high ratio of I_{ph}/n.
4. The gas cooling due to other lines. When the stellar radiation ionizing the carbon is weak, a sufficient amount of C^+ ions is not produced. In this case, the gas must be cooled through other lines, such as [C I] fine-structure and CO rotational lines. On the other hand, the [O I] 63 μm and the [Si II] 35 μm fine-structure lines can cool the gas predominantly at a high gas temperature.
5. The temperature of grains. When the dust temperature is low ($T_{\mathrm{dust}} < 20$ K) even near the cloud surface, where most of FIR continuum is emitted, $\nu f_\nu(100\ \mu\mathrm{m})$ does not trace F_{FIR} accurately. This results in a higher $F_{[\mathrm{C\,II}]}/\nu f_\nu(100\ \mu\mathrm{m})$ ratio.

4.2. Comparison with PDR models

We compare the observed flux ratios with the luminosity ratios based on the PDR models of Mochizuki & Nakagawa (2000). The model cloud is spherical and immersed in isotropic stellar light with a wavelength range of $0.0912\ \mu\mathrm{m} \le \lambda \le 8\ \mu\mathrm{m}$. Equations for chemical equilibrium and thermal balance are solved at each radius in the cloud and then line and continuum luminosities are derived. Each of the models is characterized by three parameters: cloud-illuminating UV flux (G_0) relative to the solar neighborhood value; hydrogen number density (n_{H}); mean hydrogen column density ($\langle N_{\mathrm{H}}\rangle$). Constant gas density in the cloud is assumed instead of the density structure in the original models of Mochizuki & Nakagawa (2000), to simplify discussions on the density dependence. We also use $\langle N_{\mathrm{H}}\rangle$ instead of cloud mass (M) used in the original models, in order to show the dependence of luminosity ratios on the column density more clearly. The relation between the two parameters can be written as:

$$\left(\frac{M}{10^3\ M_\odot}\right) = 2.0 \left(\frac{\langle N_{\mathrm{H}}\rangle}{10^{22}\ \mathrm{cm}^{-2}}\right)^3 \left(\frac{n_{\mathrm{H}}}{10^3\ \mathrm{cm}^{-3}}\right)^{-2} \qquad (3)$$

(e.g., Mochizuki & Nakagawa 2000) for a spherical cloud.

We modified the spectrum of the stellar radiation illuminating the model cloud in accordance with the soft radiation field in galactic centers. Nakagawa et al. (Paper I) estimated the Galactic fraction of the dust heating by the UV in that by the whole wavelength range: our Galactic center has a 3 times smaller fraction than our Galactic disk does. Accordingly, the flux at $\lambda \ge 1\ \mu\mathrm{m}$ was enhanced in the present models by a factor of 3 relative to that at $\lambda < 1\ \mu\mathrm{m}$, compared to the solar neighborhood spectrum of Mathis et al. (1983). The photoelectric heating process adopted in the Mochizuki & Nakagawa (2000) models follows the formalism by de Jong et al. (1980): only far-UV photons with energies of $h\nu \ge 6$ eV are effective.

Fig. 5 shows the luminosity ratio of $L_{[\mathrm{C\,II}]}/\nu l_\nu(100\ \mu\mathrm{m})$ as a function of $\langle N_{\mathrm{H}}\rangle$, where $L_{[\mathrm{C\,II}]}$ is the [C II] line luminosity, and $l_\nu(100\ \mu\mathrm{m})$ is the luminosity density (luminosity per unit frequency width) at a wavelength of $\lambda = 100\ \mu\mathrm{m}$, of the model cloud. The luminosity ratio is $L_{[\mathrm{C\,II}]}/\nu l_\nu(100\ \mu\mathrm{m}) = 1\text{–}2 \times 10^{-3}$ when $\langle N_{\mathrm{H}}\rangle$ is sufficiently high, the grains are neutral and sufficiently warm, and the gas is predominantly cooled by the [C II] emission (e.g., $n_{\mathrm{H}} = 10^3\ \mathrm{cm}^{-3}$ and $\langle N_{\mathrm{H}}\rangle = 10^{22}\ \mathrm{cm}^{-2}$; $n_{\mathrm{H}} = 10^4\ \mathrm{cm}^{-3}$, $\langle N_{\mathrm{H}}\rangle = 10^{22}\ \mathrm{cm}^{-2}$, and $G_0 = 10$). These lower ratios are consistent with the flux ratios observed in our Galactic center (Fig. 4), as Nakagawa et al. (Paper I) discussed for $[\mathrm{C\,II}]/40\text{–}120\ \mu\mathrm{m}$ intensity ratio as a rough estimate. On the other hand, the higher M31 ratio $F_{[\mathrm{C\,II}]}/\nu f_\nu(100\ \mu\mathrm{m}) \simeq 6 \times 10^{-3}$ can be produced when the following conditions are satisfied simultaneously:

1. $G_0/n_{\mathrm{H}} \lesssim 10^{-2}\ \mathrm{cm}^3$. This keeps the grains neutral.
2. $\langle N_{\mathrm{H}}\rangle \lesssim 10^{21}\ \mathrm{cm}^{-2}$. This makes the cloud translucent for less energetic photons.

Otherwise, the $[\mathrm{C\,II}]/100\ \mu\mathrm{m}$ ratio becomes lower (Sect. 4.1). In particular, the small $\langle N_{\mathrm{H}}\rangle$ is crucial for producing the M31 ratio under the assumed spectrum of the incident stellar light, because $G_0/n_{\mathrm{H}} \lesssim 10^{-2}\ \mathrm{cm}^3$ is satisfied for typical galactic molecular clouds (Mochizuki & Nakagawa 2000).

The gas is predominantly cooled by [C I] fine-structure or CO rotational lines, when $G_0/(n_{\mathrm{H}}\langle N_{\mathrm{H}}\rangle) \lesssim 10^{-25}\ \mathrm{cm}^5$. This can produce lower $L_{[\mathrm{C\,II}]}/\nu l_\nu(100\,\mu\mathrm{m})$ ratios as observed in our Galactic center at a lower $\langle N_{\mathrm{H}}\rangle$ (Fig. 5c) than the cases of [C II]-dominant cooling. However, this results in a too weak FIR line and continuum emission relative to the CO ($J = 1$–0) emission, compared to the observations (Dame et al. 1987; for the CO emission) toward our Galactic center. Thus, the above models rule out cooling due to those lines in our Galactic center. This indicates that the difference in the $[\mathrm{C\,II}]/100\ \mu\mathrm{m}$ ratio between

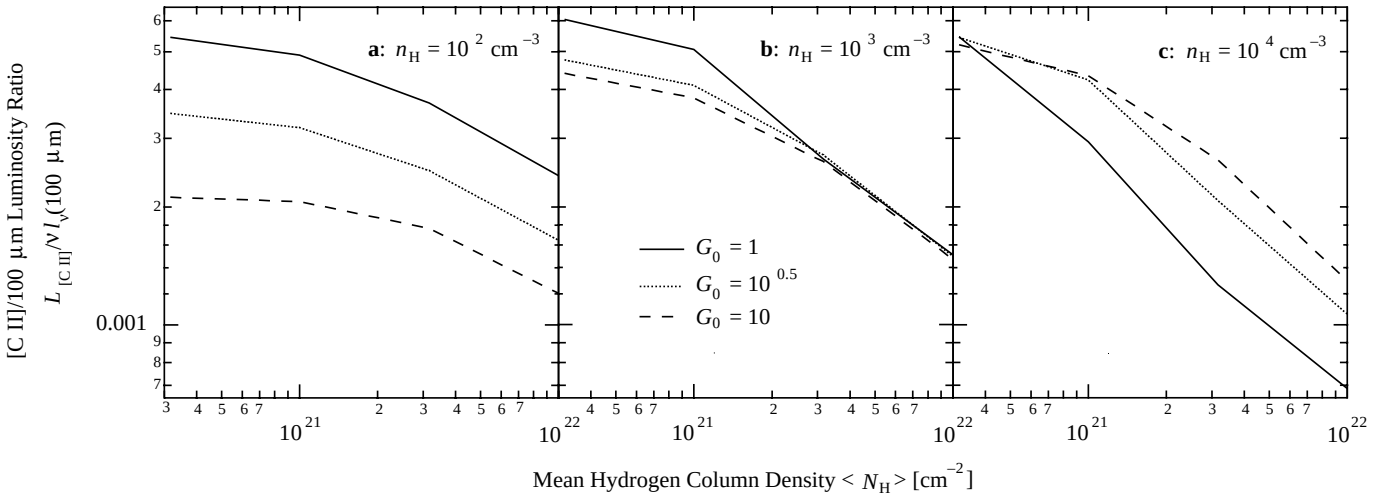

Fig. 5a–c. $[\mathrm{C\,II}]/100\ \mu\mathrm{m}$ luminosity ratio as a function of the mean hydrogen column density of the cloud. The luminosity ratio is based on the PDR models by Mochizuki & Nakagawa (2000) with the following modifications: (1) the hydrogen number density n_H is constant in the model cloud; (2) the flux of the incident stellar radiation is G_0 times the solar neighborhood value (Mathis et al. 1983) at $0.0912\ \mu\mathrm{m} \leq \lambda < 1\ \mu\mathrm{m}$, and $3G_0$ times at $1\ \mu\mathrm{m} \leq \lambda \leq 8\ \mu\mathrm{m}$. The solid, dotted, and dashed curves indicate $G_0 = 1$, $10^{0.5}$, and 10 models, respectively. **a** The assumed density is $n_\mathrm{H} = 10^2\ \mathrm{cm}^{-3}$. **b** $n_\mathrm{H} = 10^3\ \mathrm{cm}^{-3}$. **c** $n_\mathrm{H} = 10^4\ \mathrm{cm}^{-3}$.

the two galactic centers primarily results from the difference in $\langle N_\mathrm{H}\rangle$. We discuss the possibility of CO-dominant cooling further below (Sect. 4.4 and Appendix A).

The grain temperature can be less than 20 K even near the surface of the model cloud, at $G_0 \lesssim 1$. However, this effect does not account for the difference in the $[\mathrm{C\,II}]/100\ \mu\mathrm{m}$ ratio between the two galactic centers because the UV flux is not extremely low in the bulge of M31 (of the order $G_0 \sim 10^{0.5}$; Bohlin et al. 1985).

The $[\mathrm{C\,II}]/100\ \mu\mathrm{m}$ ratio and its dependence on $\langle N_\mathrm{H}\rangle$ is sensitive to the spectrum of the incident stellar light and to the photon-energy dependence of the efficiency ϵ_ph, especially to the convolution of them. Recent models indicate that a photoelectron can be emitted also by a less energetic photon (Bakes & Tielens 1994) than classically expected. Nevertheless, the decreased contribution of less energetic photons at $A_V \lesssim 1$ occurs independently of such details, as long as the stellar radiation is the heating source and the gas is heated by more energetic photons on average than the grains are. Thus, we discuss only the extreme case where the gas-to-dust heating ratio is independent of photon energy (Sect. 4.4 and Appendix A) in the present paper.

4.3. Molecular clouds in the M31 center

Loinard et al. (1995) observed the CO ($J = 1$–0) emission in the inner region of M31. The integrated main-beam temperature was $\int T_{J=1-0} dv = 0.4\ \mathrm{K\ km\ s^{-1}}$ at $x = +3'.6$ with a spatial resolution of $35''$, and no emission was detected at $x = -3'.6$. Accordingly, we adopt $\int T_{J=1-0} dv \simeq 0.2\ \mathrm{K\ km\ s^{-1}}$ for the average around $|x| = 3'.6$. Since the [C II] flux in the LWS beam is $F_{[\mathrm{C\,II}]} \simeq 5 \times 10^{-20}\ \mathrm{W\ cm^{-2}}$ there (Fig. 2a), the [C II]/CO ($J = 1$–0) line intensity ratio is $I_{[\mathrm{C\,II}]}/I_{\mathrm{CO}\ (J=1-0)} \sim 10^4$. This roughly estimated ratio is higher than the 1.3×10^3 in the inner region of our Galaxy (Nakagawa et al. 1998; Dame et al. 1987) and not lower than 6.3×10^3 as found for starburst galaxies (Stacey et al. 1991) in spite of the less active recent star formation in M31. The high [C II]/CO ($J = 1$–0) line ratio is compatible with the low column density we proposed for a M31 cloud, because the low $\langle N_\mathrm{H}\rangle$ allows incident UV photons to dissociate CO molecules in a larger fraction of the gas contained in the cloud. We will discuss the [C II]/CO ($J = 1$–0) ratio further in a forthcoming paper based on CO observations with a better sensitivity.

The central $\simeq 10\ \mathrm{kpc}$ region of M31 shows very low excitation of CO rotational transitions ($\int T_{J=2-1} dv / \int T_{J=1-0} dv \simeq 0.3$; Loinard et al. 1995). This indicates that a large fraction of the molecular gas in this region has a low density ($n_\mathrm{H} \sim 10^2\ \mathrm{cm^{-3}}$) compared to that in our Galactic disk ($n_\mathrm{H} \sim 10^3\ \mathrm{cm^{-3}}$). This decreases $\langle N_\mathrm{H}\rangle$ of M31 clouds relative to that of Galactic ones, if the typical mass of the clouds is similar between the two galaxies. When typical densities of $n_\mathrm{H} = 10^2\ \mathrm{cm^{-3}}$ and $10^3\ \mathrm{cm^{-3}}$ are adopted for M31 and Galactic clouds with the same M, respectively, the typical $\langle N_\mathrm{H}\rangle$ ratio of M31 to our Galaxy is $10^{-2/3}$ using Eq. (3). Assuming $\langle N_\mathrm{H}\rangle = 10^{22}\ \mathrm{cm^{-2}}$ in our Galaxy, we obtain $\langle N_\mathrm{H}\rangle = 2 \times 10^{21}\ \mathrm{cm^{-2}}$ in M31. These column densities are compatible with the observed difference in $F_{[\mathrm{C\,II}]}/\nu f_\nu(100\ \mu\mathrm{m})$ (Sect. 4.2).

The lower n_H in M31 can result from a lower pressure of the ISM. The ISM pressure is likely to be lower in M31 than in our Galaxy, because the lower star-forming rate in M31 leads to a lower rate of supernova explosions.

A molecular cloud has a small opacity against the incident radiation field also in a galaxy with a low dust-to-gas abundance ratio, unless the low dust abundance affects the hydrogen column density of the cloud. This may account for the relatively large FIR [C II]/continuum intensity ratios observed

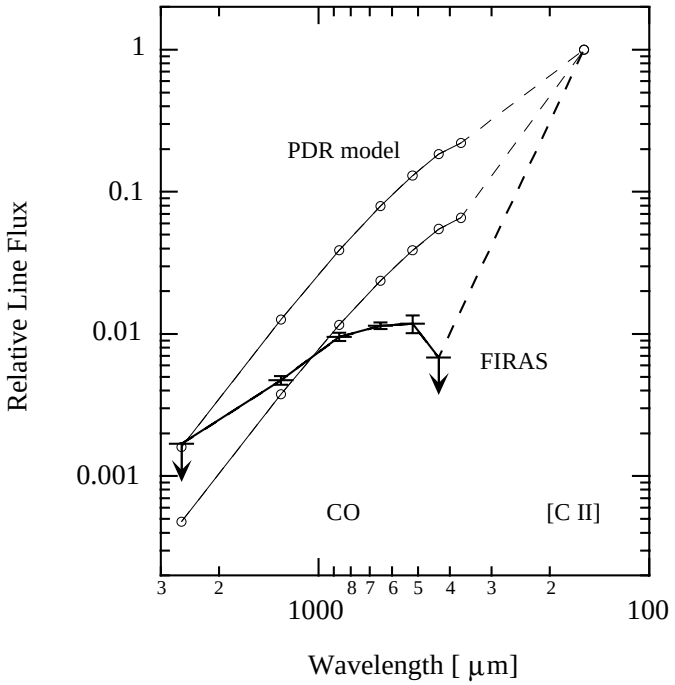

Fig. 6. Flux of the [C II] fine-structure and CO rotational lines normalized to that of the [C II] line v.s. line wavelength. The thick curve indicates FIRAS observations toward the Galactic center (Bennett et al. 1994). The error bars (1σ) and the upper limits (3σ) represent statistic uncertainties. The thin curves indicate calculations based on the PDR model described in Appendix A with $G_0 = 10$, $n_{\rm H} = 3 \times 10^4$ cm^{-3}, and $\langle N_{\rm H} \rangle = 10^{22}$ cm^{-2}. The upper and lower thin curves are for the cases where the [C II] and CO emissions originate in the same regions and where the [C II] emission fills a scale height of 370 pc (the FIRAS resolution at the distance of our Galactic center) while the CO emission is confined to that of 230 pc (the LWS resolution at the distance of M31), respectively.

(the Large Magellanic Cloud, Mochizuki et al. 1994; IC 10, Madden et al. 1997) in galaxies with low metallicities.

4.4. Gas heating due to less energetic photons

We discuss another case where the molecular clouds in M31 have a column density sufficiently high ($\langle N_{\rm H} \rangle \gtrsim 10^{22}$ cm^{-2}) to absorb the soft interstellar radiation field. In this case, the heating ratio of gas-to-dust must be insensitive to the energy of incident photons over the energy range effective for dust heating because the FIR $[\mathrm{C\,II}]/100\ \mu$m ratio observed in M31 is not decreased by the soft radiation field. Since the photon-energy dependence of the gas heating is not so well-determined as that of the dust heating, we consider in this subsection that a photoelectron can be emitted from a grain surface by a less energetic photon as well as by a UV photon.

When the photon energy effective for gas heating decreases on average, the gas-heating radiation penetrates a molecular cloud more deeply. This increases the contribution of CO rotational transitions to the gas cooling. When the cooling due to the CO emission exceeds that due to the [C II] emission, the [C II] emission does not trace the gas cooling, and consequently $L_{[\mathrm{C\,II}]}/\nu l_\nu(100\ \mu\mathrm{m})$ decreases. This CO cooling is more effective at a higher gas density because the high density enables CO molecules to survive even close to the cloud surface where the gas-heating rate is higher than inside (Appendix A).

In order to examine the influence of an energy-insensitive gas-to-dust heating ratio on the CO cooling quantitatively, we carried out calculations with PDR models under the assumption that photoelectric efficiency $\epsilon_{\rm ph}$ is independent of photon energy (Appendix A). These simulations indicate that the $[\mathrm{C\,II}]/100\ \mu$m ratio is so low as observed toward our Galactic center at $n_{\rm H} \gtrsim 3 \times 10^4$ cm^{-3} because of CO-dominant cooling. On the other hand, at lower gas densities ($n_{\rm H} \lesssim 10^3$ cm^{-3}), the models provide nearly constant ratios as high as observed in the central kiloparsec of M31 and in the general Galactic plane because of [C II]-dominant cooling. As a result, the observed difference in $F_{[\mathrm{C\,II}]}/\nu f_\nu(100\ \mu\mathrm{m})$ between the centers of M31 and our Galaxy can be reproduced by a difference in gas density.

However, the models of CO-dominant cooling are incompatible with observations of our Galactic center (Bennett et al. 1994) with the Far-Infrared Absolute Spectrophotometer (FIRAS). We averaged the line fluxes of the two FIRAS pixels centered on $l = \pm 2\overset{\circ}{.}5$, $b = 0^\circ$, to compare them with the CO-dominant cooling model described in Appendix A with parameters of $G_0 = 10$, $n_{\rm H} = 3 \times 10^4$ cm^{-3}, and $N_{\rm H} = 10^{22}$ cm^{-2} reproducing the FIR $[\mathrm{C\,II}]/100\ \mu$m ratio observed toward our Galactic center (Fig. 6). Each of the FIRAS pixels represents a line flux averaged over a $5^\circ \times 5^\circ$ region (Bennett et al. 1994) while we discuss CO cooling at the scale height displayed in Figs. 2 and 4, $|b| \leq 0\overset{\circ}{.}7$ (corresponding to the LWS beam at the distance of M31). Since the [C II] emission may be extended beyond the regions where the CO emission dominates the gas cooling, we consider two limits in the distribution of emission. In one limit, the [C II] and CO emissions have the same scale heights. In the other, the [C II] emission is uniformly distributed in the FIRAS pixels, while the CO emission is confined to $|b| \leq 0\overset{\circ}{.}7$. Fig. 6 shows that the observed mid-J CO lines are too weak compared to the model of CO-dominant cooling independently of the assumed emission distribution. Thus, the CO-dominant cooling is unlikely in our Galactic center, at least on the scale of kpc.

The exclusion of the CO-dominant cooling is insensitive to compared models, because the observed line fluxes directly restrict the energy carried away by the CO lines. We therefore conclude that the difference in $F_{[\mathrm{C\,II}]}/\nu f_\nu(100\,\mu\mathrm{m})$ between the two galactic centers is due to the difference in typical column density of clouds.

4.5. [C II] self-absorption

The edge-on view of our Galaxy may result in a large optical depth of the [C II] line toward our Galactic center. On the other hand, the [C II] opacity is unlikely to be large toward the M31 center, which contains a much smaller amount of the neutral ISM than the Galactic counterpart does. This suggests that the self-absorption of the line may cause the difference in the

$[\mathrm{C\,II}]/100\ \mu\mathrm{m}$ ratio between the two galaxies. However, Nakagawa et al. (Paper I), who estimated the line opacity toward our Galactic center, concluded that this effect is insignificant. In the following, we discuss a few points supporting Paper I.

1. Nakagawa et al. (Paper I) compared the Galactic [C II] emission also to the CO ($J = 1$–0) emission (Dame et al. 1987). The CO emission does not show a deficit toward our Galactic center unlike the [C II] emission, although the former line generally has a much larger optical depth.
2. Sauty et al. (1998) simulated the [C II] line and the $100\ \mu\mathrm{m}$ continuum emission for the edge-on galaxy NGC 891, assuming distributions of the molecular clouds and the UV sources in the galaxy. Their results showed a [C II] optical depth of $\tau_{[\mathrm{C\,II}]} = 0.4$, not large enough compared to the deficit in the $[\mathrm{C\,II}]/100\ \mu\mathrm{m}$ ratio (a factor of 2–3) toward our Galactic center.
3. Madden et al. (1993) observed the distribution of the [C II] emission in NGC 6946. This galaxy also shows a [C II] deficit relative to the FIR continuum toward its center in spite of its face-on view, although the limited spatial resolution (2.7 kpc when a distance of 10.1 Mpc is adopted) prevents a quantitative comparison to our Galactic center.

5. Conclusions

We observed the nearby spiral M31 with the LWS on board the ISO at the central 5 kpc ($1500''$) region along the major axis of the galaxy. The [C II] $158\ \mu\mathrm{m}$ line emission was detected in the inner 1.6 kpc, as well as the FIR continuum. The obtained FIR line-to-continuum ratio is $F_{[\mathrm{C\,II}]}/\nu f_\nu(100\ \mu\mathrm{m}) \simeq 6 \times 10^{-3}$, 2–3 times higher than that in the Galactic counterpart and close to that in the general Galactic plane.

We compared the observations with PDR models, taking into account the soft interstellar radiation field due to the late-type stars in galactic bulges. Since the grains are heated by less energetic photons on average than the gas is, the soft radiation field produces so low FIR $[\mathrm{C\,II}]/100\ \mu\mathrm{m}$ ratios as observed toward our Galactic center, when the model cloud has a sufficiently high column density ($\langle N_\mathrm{H}\rangle \gtrsim 10^{22}\ \mathrm{cm}^{-2}$). However, the models provide higher $[\mathrm{C\,II}]/100\ \mu\mathrm{m}$ ratios at $\langle N_\mathrm{H}\rangle \lesssim 10^{21}\ \mathrm{cm}^{-2}$, because the cloud becomes translucent for photons sufficiently energetic to heat the grains but not sufficiently energetic to heat the gas. This is a likely mechanism causing the relatively high $[\mathrm{C\,II}]/100\ \mu\mathrm{m}$ ratios in the central region of M31 in spite of its bright bulge.

Previous millimeter observations suggest that a large fraction of the molecular gas has a low density ($n_\mathrm{H} \sim 10^2\ \mathrm{cm}^{-3}$) in the inner ten kiloparsecs of M31. This decreases $\langle N_\mathrm{H}\rangle$ of M31 clouds relative to that of Galactic ones, if the typical masses of clouds are similar between the two galaxies. A lower gas density can result from a lower pressure of the ISM in a galaxy; the inner region of M31 is likely to have a low ISM pressure because of its low recent star-forming activity.

The [C II] deficit previously observed toward our Galactic center may be attributed to the dominance of CO rotational transitions in the cooling of the neutral gas. However, FIRAS observations show that the CO emission toward our Galactic center is too weak for the CO-dominant cooling, at least on the scale of kpc. The self-absorption of the [C II] line toward our Galactic center is also unlikely to account for the [C II] deficit, as previously estimated. We therefore conclude that the difference in the $[\mathrm{C\,II}]/100\ \mu\mathrm{m}$ ratio between the two galactic centers is due to the difference in the column density of a molecular cloud.

Acknowledgements. K. M. was financially supported by a Research Fellowship of the Japan Society for the Promotion of Science for Young Scientists.

Appendix A: gas cooling due to CO molecules

First we discuss conditions for a molecular cloud cooled predominantly by the CO rotational transitions, considering a simplified situation as follows. (1) The cloud has a sufficiently high column density to absorb the incident radiation over the wavelength range effective to the dust heating. (2) The dominant form of gas-phase carbon is C^+ ion near the surface of the cloud, and CO molecule inside. We define the C^+–CO transition column density, $N_\mathrm{H}^\mathrm{transit}$, as the hydrogen column density from the surface to the region where C^+ and CO are equally abundant. (3) The gas is cooled by the [C II] fine-structure line at $N_\mathrm{H} \le N_\mathrm{H}^\mathrm{transit}$ and by the CO rotational lines at $N_\mathrm{H} > N_\mathrm{H}^\mathrm{transit}$, where N_H is the hydrogen column density from the surface. Under these assumptions, the cooling due to the CO lines exceeds that due to the [C II] line for the whole cloud, when the energy input to the gas is larger in the CO region than in the C^+ region: $N_\mathrm{H}^\mathrm{heat} > N_\mathrm{H}^\mathrm{transit}$, where $N_\mathrm{H}^\mathrm{heat}$ is the hydrogen column density characteristic for the attenuation of the gas-heating radiation.

The column density $N_\mathrm{H}^\mathrm{transit}$ is determined by the chemical balance between the two cooling species. The conversion rate ($r_{\mathrm{CO}\to\mathrm{C}^+}$; events per unit time per unit volume) of $\mathrm{CO} \to \mathrm{C}^+$ as a function of N_H can be approximately written as:

$$r_{\mathrm{CO}\to\mathrm{C}^+}(N_\mathrm{H}) = G_0 \alpha_\mathrm{CO}^0 n_\mathrm{CO}(N_\mathrm{H}) \exp\left(-\frac{N_\mathrm{H}}{N_\mathrm{H}^\mathrm{UV}}\right), \qquad \text{(A.1)}$$

where α_CO^0 is the photodissociation rate of CO molecule at the unattenuated radiation field of $G_0 = 1$, $n_\mathrm{CO}(N_\mathrm{H})$ is the number density of CO molecule as a function of N_H, and N_H^UV is the hydrogen column density characteristic for the attenuation of the CO-dissociating UV radiation. On the other hand, the rate ($r_{\mathrm{C}^+\to\mathrm{CO}}$) of $\mathrm{C}^+ \to \mathrm{CO}$ conversion, which consists of two-body collisions in the gas, can be approximately written as:

$$r_{\mathrm{C}^+\to\mathrm{CO}}(N_\mathrm{H}) = k_{\mathrm{C}^+} n_\mathrm{H} n_{\mathrm{C}^+}(N_\mathrm{H}), \qquad \text{(A.2)}$$

where k_{C^+} is the total rate coefficient of the $\mathrm{C}^+ \to \mathrm{CO}$ reactions, and $n_{\mathrm{C}^+}(N_\mathrm{H})$ is the number density of C^+ ion. The chemical balance is achieved by equating the two conversion rates: $r_{\mathrm{CO}\to\mathrm{C}^+} = r_{\mathrm{C}^+\to\mathrm{CO}}$. At the C^+–CO transition zone, where $n_{\mathrm{C}^+}(N_\mathrm{H}) = n_\mathrm{CO}(N_\mathrm{H})$,

$$N_\mathrm{H}^\mathrm{transit} = N_\mathrm{H}^\mathrm{UV} \ln\left(\frac{\alpha_\mathrm{CO}^0}{k_{\mathrm{C}^+}} \frac{G_0}{n_\mathrm{H}}\right) \qquad \text{(A.3)}$$

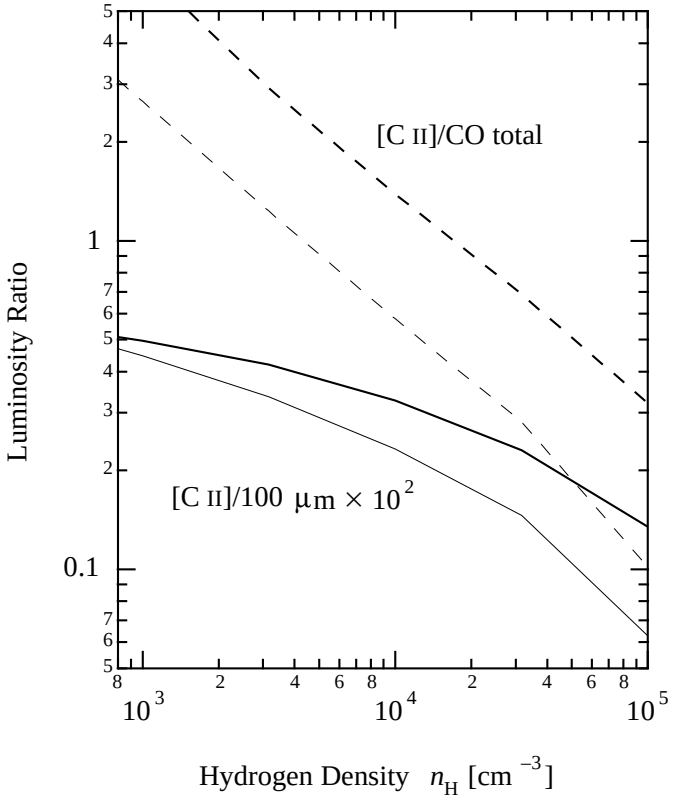

Fig. A.1. Line and continuum luminosity ratios based on PDR models as a function of hydrogen number density, $n_{\rm H}$, of the model cloud. The assumed photoelectric efficiency is 6×10^{-3}, independent of the energy of the incident photons. Otherwise, the models are equivalent to those for Fig. 5. The solid curves indicate the FIR luminosity ratio ($L_{[\rm C\,II]}/\nu l_\nu[100\ \mu{\rm m}]$, multiplied by 10^2) of the [C II] line to the 100 μm continuum. The dashed curves indicate $L_{[\rm C\,II]}/L_{\rm CO\,total}$, where $L_{\rm CO\,total}$ is the total luminosity of the CO rotational lines. Thin and thick curves are for $G_0 = 10^{0.5}$ and 10, respectively. The mean hydrogen column density of the cloud is assumed to be $\langle N_{\rm H}\rangle = 10^{22}\ {\rm cm}^{-2}$.

is obtained (e.g., Mochizuki & Onaka 2000). As a result, the condition of CO-dominant cooling can be written as:

$$\ln\left(\frac{\alpha_{\rm CO}^0}{k_{\rm C^+}}\frac{G_0}{n_{\rm H}}\right) < \frac{N_{\rm H}^{\rm heat}}{N_{\rm H}^{\rm UV}}. \qquad \text{(A.4)}$$

This condition can be satisfied by a small $G_0/n_{\rm H}$ and/or a large $N_{\rm H}^{\rm heat}$. The latter requires (1) a small lower limit of photon energy capable of heating the gas and (2) soft cloud-illuminating radiation.

For more quantitative discussion, we calculated line and continuum ratios based on PDR models involving gas heating due to less energetic photons. In these models, we assumed an extreme case where photoelectric efficiency is a constant of 6×10^{-3}, which represents the $I_{[\rm C\,II]}/I_{\rm FIR}$ in the Galactic plane (Nakagawa et al. 1998), independent of photon energy. Except this assumption, the models are equivalent to those described in Sect. 4.2. The total cooling due to the CO rotational lines exceeds the cooling due to the [C II] line, at $n_{\rm H} \gtrsim 10^4\ {\rm cm}^{-3}$, as shown in Fig. A.1 for $G_0 = 10^{0.5}$ and 10. In this case, the [C II] emission does not trace the gas heating, and consequently $L_{[\rm C\,II]}/\nu l_\nu(100\ \mu{\rm m})$ is smaller than in the case of [C II]-dominant cooling. According to the above models, the different $F_{[\rm C\,II]}/\nu f_\nu(100\ \mu{\rm m})$ ratios observed between the two galactic centers can be reproduced by the difference in gas density (Sect. 4.4).

The gas-to-dust heating ratio can be insensitive to photon energy when the gas heating is dominated by the photoelectric effect through negatively-charged smaller particles (large molecules) such as Polycyclic Aromatic Hydrocarbon (PAH) anions rather than through grains, because small electron affinities of these anions allow a photoelectron to be emitted by a less energetic (~ 1 eV) photon. Lepp & Dalgarno (1988) estimated that the large molecules heat the gas predominantly when the abundance of these molecules exceeds 2×10^{-7} relative to that of hydrogen. One fifth of this abundance was suggested for carbon chain anions C_7^- in the Galactic ISM on the basis of diffuse infrared band (DIB) observations (Tulej et al. 1998). Since PAH molecules are more stable than these carbon chain molecules, the PAH anions may be abundant sufficiently in the ISM. Moreover, Uchida et al. (1998) found that the excitation of the infrared emission features (IEFs), which is often considered to be radiated from large molecules (e.g., Léger & Puget 1984), cannot be accounted for only by the absorption of UV photons; they proposed the absorption of visible photons for the additional excitation. The excitation due to visible photons may result from negative charge of the IEF carriers, because a large molecule can absorb a less energetic photon when it is ionized (Allamandola et al. 1989) than when neutral.

References

Allamandola L.J., Tielens A.G.G.M., Barker J.R., 1989, ApJS 71, 733
Bakes E.L.O., Tielens A.G.G.M., 1994, ApJ 427, 822
Bennett C.L., Fixsen D.J., Hinshaw G., et al., 1994, ApJ 434, 587
Bohlin R.C., Cornett R.H., Hill J.K., et al., 1985, ApJ 298, L37
Brinks E., Shane W.W., 1984, A&AS 55, 179
Clegg P.E., Ade P.A.R., Armand C., et al., 1996, A&A 315, L38
Dame T.M., Ungerechts H., Cohen R.S., et al., 1987, ApJ 322, 706
Dame T.M., Koper E., Israel F.P., Thaddeus P., 1993, ApJ 418, 730
de Jong T., 1977, A&A 55, 137
de Jong T., Dalgarno A., Boland W., 1980, A&A 91, 68
Heiles C., 1994, ApJ 436, 720
Kessler M.F., Steinz J.A., Anderegg M.E., et al., 1996, A&A 315, L27
Léger A., Puget J.L., 1984, A&A 137, L5
Lepp S., Dalgarno A., 1988, ApJ 335, 769
Lloyd C., 1999, LWS Instrument Team Report 1999 September, RAL, Didcot
Loinard L., Allen R.J., Lequeux J., 1995, A&A 301, 68
Madden S.C., Geis N., Genzel R., et al., 1993, ApJ 407, 579
Madden S.C., Poglitsch A., Geis N., Stacey G.J., Townes C.H., 1997, ApJ 483, 200
Martinez Roger C., Phillips J.P., Sanchez Magro C., 1986, A&A 161, 237
Mathis J.S., Mezger P.G., Panagia N., 1983, A&A 128, 212
Mochizuki K., Nakagawa T., 2000, ApJ 535, 118
Mochizuki K., Onaka T., 2000, A&A, submitted
Mochizuki K., Nakagawa T., Doi Y., et al., 1994, ApJ 430, L37

Nakagawa T., Doi Y., Yui Y.Y., et al., 1995, ApJ 455, L35 (Paper I)
Nakagawa T., Yui Y.Y., Doi Y., et al., 1998, ApJS 115, 259
Rice W., 1993, AJ 105, 67
Sauty S., Gerin M., Casoli F., 1998, A&A 339, 19
Shibai H., Okuda H., Nakagawa T., et al., 1991, ApJ 374, 522
Stacey G.J., Geis N., Genzel R., et al., 1991, ApJ 373, 423
Swinyard B.M., Burgdorf M.J., Clegg P.E., et al., 1998, Proc. SPIE 3354, 888
Tielens A.G.G.M., Hollenbach D.J., 1985, ApJ 291, 722
Tulej M., Kirkwood D.A., Pachkov M., Maier J.P., 1998, ApJ 506, L69
Uchida K.I., Sellgren K., Werner M., 1998, ApJ 493, L109
Walterbos R.A.M., Schwering P.B.W., 1987, A&A 180, 27
Wheelock S.L., Gautier T.N., Chillemi J., et al., 1994, *IRAS* Sky Survey Atlas Explanatory Supplement, JPL Publication 94-11, JPL, Pasadena
Xu C., Helou G., 1994, ApJ 426, 109